Synergetic Exterior and Interfacial Approaches by Colloidal Carbon Quantum Dots for More Stable Perovskite Solar Cells Against UV

Dongjiu Zhang, Zhelu Hu, Sergio Vlaic, Chenghao Xin, Stéphane Pons, Laurent Billot, Lionel Aigouy, Zhuoying Chen

Synergetic Exterior and Interfacial Approaches by Colloidal Carbon Quantum Dots for More Stable Perovskite Solar Cells Against UV†

Dongjiu Zhang, Zhelu Hu,# Sergio Vlaic, Chenghao Xin, Stéphane Pons, Laurent Billot, Lionel Aigouy and Zhuoying Chen*

[1.] Laboratoire de Physique et d'Etude des Matériaux (LPEM), ESPCI Paris, PSL University, Sorbonne Université, CNRS UMR 8213, 10 Rue Vauquelin, F-75005 Paris, France

Abstract.

The achievement of both efficiency and stability in perovskite solar cells (PSCs) remains a challenging and actively researched topic. In particular, among different environmental factors, ultraviolet (UV) photons play a pivotal role contributing to device degradation. In this work, by harvesting simultaneously both the optical and the structural properties of bottom-up-synthesized colloidal carbon quantum dots (CQDs), we provide a cost-effective means to circumvent the UV-induced degradation in PSCs without scarification on their power conversion efficiencies (PCEs). By exploring and optimizing the amount of CQDs and the

† Electronic supplementary information (ESI) available: Fig. S1–S8: PLQE measurement results of the CQDs; PL mapping experiment descriptions and results of the different CQD layers achieved under configuration I; The current-voltage (*J-V*) characteristics comparing PSCs without and with CQDs (configuration II) of much larger CQD quantities than to those shown in the main text; Sheet resistance characterizations; EDX elemental mapping results and analysis; The perovskite grain size distribution measured by SEM; Solar cell degradation behavior under continuous UV illumination; J-V and degradation results on triple-cation mixed halide PSCs. Table S1-S4: Summary of the average photovoltaic parameters measured on the PSCs with CQDs coated under configuration I; Summary of the best and the average photovoltaic parameters of the J-V characteristics on the PSCs with CQDs inserted under configuration II. Summary of the PCEs achieved previously on representative high-efficiency FAMA-based PSCs.

Present address: Key Laboratory of Flexible Electronics (KLOFE) & Institute of Advanced Materials (IAM), School of Flexible Electronics (Future Technologies), Nanjing Tech University, Nanjing 211816, China

* Corresponding author. Email address: zhuoying.chen@espci.fr (Z. Chen).

different location/interfaces of the solar cells where CQDs are applied, we achieve a synergetic configuration where the photovoltaic performance drop due to optical loss is completely compensated by the increased perovskite crystallinity due to interfacial modification. As a result, on the optimized configurations where CQDs were applied both on the exterior front side as an optical layer and at the interface between the electron transport layer and the perovskite absorber, PSCs with PCEs > 20% are fabricated which can maintain up to ~ 94% of their initial PCE after 100 hours of degradation in ambient air under continuous UV illumination (5 mW cm^{-2}).

I. Introduction.

The device stability issue has been currently considered as one of the bottle-necks preventing the further development of perovskite solar cells (PSCs), an emerging solution-processed photovoltaic technology based on organo-metal halide compounds with a perovskite-type crystal structure.[1–5] Among different environmental factors, ultraviolet (UV) photons play a pivotal role contributing to device degradation.[6–8] The UV radiation from the sun, conventionally refers to photons with a wavelength shorter than 400 nm, counts for approximately 5% in the terrestrial solar spectrum.[9] While such a contribution is small, it is sufficient to cause device degradation. For example, detrimental effect, activated by the UV photons available under 1-sun illumination, was observed and attributed to the interfacial reactions between the electron transport layer (ETL) based on titanium dioxide (TiO_2) and the perovskite absorber layer.[10,11] Pioneer works in this field mainly suggested two possible mechanisms, both activated by UV, either based on the interfacial perovskite decomposition induced by the TiO_2 photocatalyst,[10] or the formation of unfilled oxygen vacancy sites on the surface of TiO_2 serving as deep traps leading to losses of the photoinduced carriers.[11] The latter mechanism has led to a worse degradation observed in encapsulated devices than

unencapsulated ones due to the passivation effect of oxygen.[11] The detrimental effect of UV photons on PSCs is unfortunately not restricted only to the use of TiO_2 ETL nor the $MAPbI_3$ perovskite composition. Severe UV-induced degradation was also observed in state-of-the-art solar cells with a SnO_2 ETL and various perovskite compositions, such as triple-cation/mixed halide perovskite [12] and $FAPbI_3$[13]. Last but not the least, on "inverted *p-i-n*" PSCs [14], the applied ETL is typically based on PCBM ([6,6]-Phenyl-C_{61}-butyric acid methyl ester) which also suffers significantly from UV-induced oligomerization.[15] All above-mentioned observations therefore motivates the research community to seek for a cost-effective means to circumvent the UV-induced degradation in PSCs.

Toward this objective, in the literature there exists mainly two strategies: The first one relies on the application of photoluminescent materials to decrease the proportion of high energy UV photons of the solar spectrum to reach PSCs.[16] In comparison with a simple longpass filter which can achieve the same objective but inevitably leading to a photocurrent loss, photoluminescent materials can down-convert and down-shift the UV photons into lower energy photons which are harvestable by the solar cell. For example, a luminescent downshifting (LDS) coating based on ($Sr_4Al_{14}O_{25}:Mn^{4+}$, 0.5% Mg) phosphor particles embedded in PMMA (polymethylmethacrylate) was successfully applied in the exterior (*i.e.* on the glass side, below termed as "front side") of the FTO/glass substrate of $MAPbI_3$ PSCs leading to enhanced device stability against UV.[17] Remarkably, a Lumogen F Violet 570-doped photocurable fluoropolymer layer (developed by BASF) was applied on both the exterior front and back side of mixed cation mixed halide PSCs which can withstand harsh degradation conditions thanks to both the UV LDS and the hydrophobic properties of the fluoropolymer.[18] Besides the above-mentioned examples, rare-earth-based luminescent materials capable to downconvert UV photons have also been actively investigated.[19–21] The application of a layer of phosphor-in-glass (PiG) based on $Lu_3Al_5O_{12}:Ce^{3+}$ and $SiAlON:Eu^{2+}$ on the front side of

$MAPbI_3$ solar cells was shown to slow down device degradation under UV illumination.[22] Notably, $SrAl_2O_4$: Eu^{2+}, Dy^{3+} (SAED) nanophosphor was introduced in the interior of $MAPbI_{3-x}Cl_x$ solar cells which demonstrated superior functionality against UV aging.[23] In contrast to this first strategy which involves mainly light management, there exist another strategy which is based on the interfacial modification or the replacement of the photocatalytic metal-oxide carrier transport layer by other semiconductors. For instance, different less photoactive electron and hole transport layers were experimented, including lanthanum-doped $BaSnO_3$,[24] 2D titania atomic sheets,[25], and $CuCrO_2$ nanocrystals.[26] Interfacial modification and passivation approaches can also be achieved by applying materials such as silane coupling agents[27], CsCl[28], CsBr[29], and benzotriazole derivatives,[30] all of which allow one to keep the state-of-the-art device structures without replacing the transport layers already optimized in the field but offer reduced photocatalytic properties and electronic defect density.

In this work, we propose a combined optical and interfacial approach to harvest simultaneously the superior optical and surface properties of solution-processed luminescent carbon quantum dots (CQDs) for more stable mixed-cation PSCs against UV. These bottom-up-synthesized CQDs are nanoparticles (NPs) with carbon cores based on sp^2 domains but with a high degree of disordering together with heteroatom doping and rich surface chemical groups both of which tailor their final optical properties.[31–35] They can be synthesized through hydrothermal routes with water as the solvent under mild temperature (≤ 200 °C) by various carbon-source reactants obtainable from bioresources (e.g. citric acid,[36,37] orange peels,[38] water hyacinth leaves,[39] and pomegranate[40]). They therefore belong to a new class of low-cost fluorescent NPs based on one of the most abundant elements in the world. The optical property of CQDs, more specifically their LDS property that absorbs UV photons and re-emits in the visible spectrum, has attracted much interest for the field of photovoltaics.[41–43] Nevertheless, on PSCs, most previous reports focused only on PCE optimizations without

information in terms of the degree of UV-filtering and more importantly without demonstration on any obtainable device stability enhancement against UV illumination. For example, a LDS layer of CQDs was applied on the front side of PSCs based on γ-$CsPbI_3$[44] and triple-cation perovskite[45,46] but no evaluation on the device stability was given. On $MAPbCl_xI_{1-x}$ solar cells, Jin et al. applied CQDs as a LDS layer on the surface of mp-TiO_2 ETL and observed increased PCE and better device stability.[47] Nevertheless, it remains unclear to what extent the LDS property of CQDs really play a role in the observed phenomena as the optimized CQD-decorated-TiO_2 sample exhibit limited changes in terms of optical absorption when compared to the pristine TiO_2 sample in the UVA spectrum (*i.e.* from where > 90% of UV photons come [48]). Benetti et al. also applied CQDs as a LDS layer on the front side of $MAPbI_3$ solar cells.[49] But the optical absorption of these CQDs significantly extends in the visible spectrum which limits their usage (and UV filtering capacity). In parallel, instead of harvesting the optical property of CQDs, several studies revealed that CQDs can serve as highly valuable interfacial and/or bulk modifiers to enhance the performance of PSCs, e.g. via passivating defects and graine boundaries, [50–54], or increasing the carrier mobility of the transport layer,[55,56] or enhancing the interfacial property, morphology, and electronic coupling between the transport layer and the perovskite absorber.[49,57–61] Herein, on PSCs based on $FA_{1-x}MA_xPbI_3$, we focus in particular on their UV-induced instability and methods based on CQDs to mitigate this undesirable characteristic. We propose a combined optical and interfacial approach by which both the LDS and interfacial benefits of colloidal CQDs can be harvested to the maximum extent towards a better photovoltaic performance and in particular a more robust device stability against UV-induced degradation.

2. Results and Discussion

2.1. Configuration I: CQD as an external LDS layer

In this section, we explore the possibility to harvest the UV absorbing and LDS property of CQDs by placing them on the external front side of $FA_{1-x}MA_xPbI_3$ PSCs (schematic shown in Figure 1(a)). The fluorescent CQDs under study, with an average diameter of about 5 nm (Fig. 1(b)), were synthesized according to a previously published method[37], by which the nitrogen-containing reactant (ethylenediamine) leads to nitrogen-doping in these CQDs and a resultant intense blue fluorescence under UV excitation (Fig. 1(c)) with a photoluminescence (PL) quantum yield of about 60% (Fig. S1 of the supporting information). From their optical absorbance, a strong and broad absorption peak was observed centered at $\lambda \approx 350$ nm, which suggests their potentials in terms of UV-blockage for the solar cells (Fig. 1(d)). Part of the absorbed UV photons can contribute to the light harvesting of the solar cells by PL as shown in the $\lambda_{excitation}$-dependent PL characteristics (Fig. 1(d)). Various amounts of CQDs were then applied onto the exterior front (glass)-side of the FTO/glass substrates to build PSCs. This leads to a relatively homogenous coatings as shown in Fig. 1(e) of different thickness. The optical transmittance of these CQD-coated substrates are shown in Fig. 1(f), which exhibit a monotonic transmittance decrease in the UV spectrum as the thickness CQD layer increases. In comparison to bare FTO/glass substrates, about 46%, 77% and 84% of transmittance reduction in the UV spectrum between $\lambda = 300$ nm to 400 nm was obtained by applying a CQD coating of thickness ~ 1.15 ± 0.10, 1.66 ± 0.08, and 2.41 ± 0.13 μm, respectively (Fig. 1(e)). Besides the transmission reduction in the UV, due to the optical absorption "tail" of these CQDs extending at wavelengths longer than $\lambda = 400$ nm, there are respectively about 3.8%, 12.6%, and 19.9% of transmittance reduction in the visible spectrum ($\lambda = 400$ - 800 nm) compared to the bare substrate for the above-mentioned three different loading of CQDs (Fig. 1(e)). PL imaging was applied to examine the existence and the homogeneity of the CQD coating (Fig. 1(f) and Fig. S2). As shown in Fig. S2, no obvious clusters or PL inhomogeneity was observed on these CQD-coated samples and the intensity of the PL signal increases monotonically as the

CQD loading increases. A mechanical scratch was purposefully made on one of the CQD films with a 1.15-µm-thickness (Fig. 1(e)). The PL images and the resultant PL line profile after the scratch evidences well the presence of these CQD layers (Fig. 1(f) and Fig. S2).

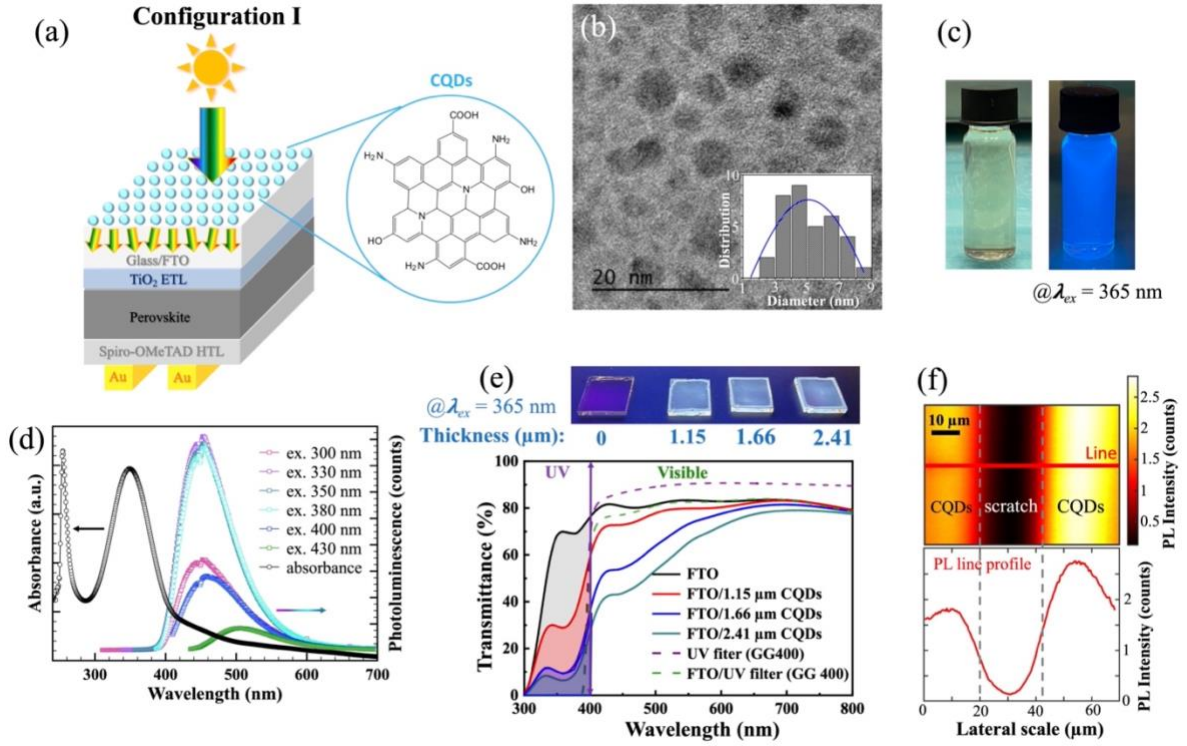

Figure 1. *(a) Schematic of the configure I under study where CQDs were deposited as a UV-absorbing and luminescent downshifting (LDS) layer on the exterior font side of the perovskite solar cell (PSC). (b) Transmission electron microscopy (TEM) image of the CQDs. Inset exhibits their size distribution. (c) Images of a bottle of CQD solution under room light (left image) and under the illumination of a UV lamp at λ = 365 nm (right image). (d) The optical absorbance and photoluminescence (PL) characteristics of the CQD solution under different excitation wavelengths. (e) The images (under λ_{UV} = 365 nm) and the optical transmittance of different glass/FTO substrates with their front (glass) sides covered by a CQD layer with an average thickness of 1.15±0.10, 1.66±0.08, and 2.41±0.13 µm. The optical transmittance of a commercial UV filter with a cut-on wavelength at 400 nm (GG 400, Thorlabs) is plotted together for comparison. (f) The PL images of a glass/FTO substrate with its front sides covered by a 1.15-nm-thick CQD layer (under $\lambda_{excitation}$ = 405 nm; PL signal collected from a 40-nm-wavelength window centered at λ = 536 nm), together with a scratch purposefully made to remove the CQDs in the middle of*

the image. The PL images of the glass/FTO substrates with CQD layer thickness are shown in the supporting information.

While it is feasible to employ a commercial UV filter to enhance stability against UV (refer to the "stability" section 2.3 below), it comes at the cost of reductions in short-circuit photocurrent (J_{sc}) and PCE. In comparison, we found that a thin fluorescent CQD layer on the front side of the PSCs is move advantageous than a commercial UV filter in terms of photocurrent loss with equivalent capability to provide device stability improvement. Here, functional PSCs were fabricated by applying a bare FTO substrate ("control" device) and the above-mentioned FTO substrates with front side covered by CQD layers of different thickness. On the control devices, the configurations with and without a commercial UV filter ($\lambda_{cut\text{-}on}$ = 400 nm) were also measured in order to observe the impact of UV filtering on the photocurrent loss and device stability. Fig. 2(a) exhibits the cross-sectional SEM image of a typical control device exhibiting its *n-i-p* type device architecture. The best current-voltage (*J-V*) characteristics measured under simulated AM1.5G 1-sun illumination (100 mW cm^{-2}) and the corresponding external quantum efficiency (EQE) spectra are shown in Fig. 2(b) and 2(c) with the averaged photovoltaic parameters and their standard distributions tabulated in Table S1. On the same control device, the fact of filtering nearly all UV photons with $\lambda < 400$ nm by a commercial UV filter (optical transmittance shown in the green dashed curve in Fig. 1(e)) led to a ~ 8.6 % reduction in terms of J_{sc} and a resultant ~ 12.5 % reduction in PCE. In comparison to the commercial UV filter, the configuration of a 1.15-μm-thick CQD layer covering the front side of the device exhibits a smaller J_{sc} and PCE reduction of ~ 6.7 % and ~ 9.8 %, respectively. Configurations with thicker CQD films were also experimented which led to a further J_{sc} reduction likely due to the stronger parasitic optical absorption tail of CQDs which extends to the visible spectrum at high CQD loading.

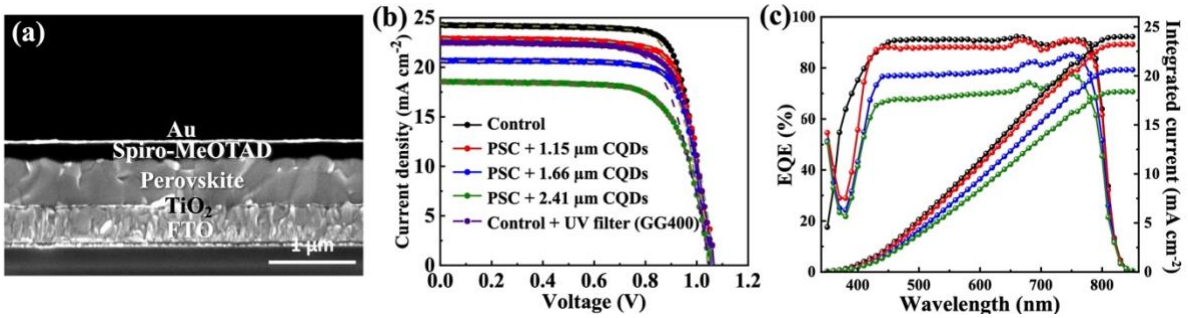

Figure 2. *(a) Cross-sectional SEM image displaying the different layers involved in the device architecture of a control PSC based on $FA_{1-x}MA_xPbI_3$. (b) The current density - voltage (J-V) characteristics comparing PSCs with their front sides covered by CQD layers of different thickness and those measured on a control device (without CQDs, without and with a commercial UV filter ($\lambda_{cut\text{-}on}$ = 400 nm, GG 400)). These J-V characteristics were measured under simulated AM1.5G solar illumination operated at 1-sun condition (at 100 mW cm^{-2}). Solid dots and lines represent the reverse scan (from V_{oc} to 0 V) and the dashed lines present the forward scan (from 0 V to V_{oc}). (c) External quantum efficiency (EQE) spectra of the different solar cells displayed in (b) together with their integrated photocurrent density.*

2.2. Configuration II: CQDs as an internal interfacial modifier

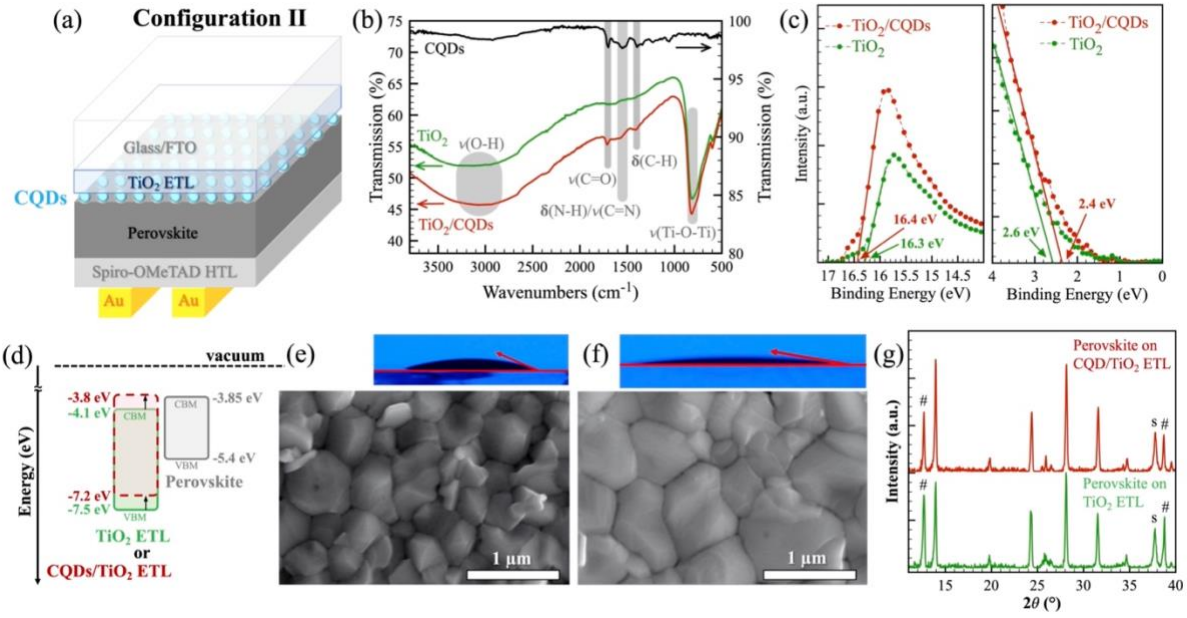

Figure 3*. (a) Schematic of configuration II: Different volumes of CQD solutions were deposited by dynamic spin-coating leading to different degrees of CQD-decoration at the ETL/perovskite interface of the PSCs. (b) FT-IR spectra measured on 50-µL-CQD-decorated TiO_2 ETL, bare TiO_2 ETL, and the same volume of CQDs deposited*

on FTO/glass substrates (without ETL). (c) The secondary electron cutoff region (left) and the Fermi edge region (right) of the ultraviolet photoelectron spectroscopy (UPS) spectra of TiO_2 ETLs with and without CQDs decorated on-top. The light source of UPS is a He1 discharge lamp (hv = 21.22 eV). (d) Schematic of the energy levels of the TiO_2 ETL with and without CQDs together with the perovskite absorber. (e, f) The water contact angle measured on (e) bare TiO_2 ETL and (f) CQD-decorated TiO_2 ETL together with the corresponding top-view SEM image of the perovskite layer grown on top. (g) XRD spectra of the perovskite layer grown on the bare TiO_2 ETL (green) and on the CQD-decorated ETL (red).

As discussed in the previous section, while being a promising method to improve the device stability against UV, the method of covering the front-sides of PSCs by CQDs exhibits some inconvenience in terms of J_{sc} and PCE drops due to optical loss. Here, we thus explored another configuration where we inserted CQDs at the ETL/absorber interface and we investigated their impacts on the photovoltaic property and stability. Unlike the previous configuration I, where continuous CQD films were formed, here, dynamic spin-coating was applied which resulted in only scarce amounts of CQDs at the interface. This was done purposefully in order to avoid the formation of any continuous CQD film at the ETL/absorber interface as we observed a loss of J_{sc} when relatively large amounts of CQDs were applied at the interface (Fig. S3). This is coherent with the sheet resistance (R_{SH}) measurements performed on a continuous CQD film on which highly resistive behavior ($R_{SH} > 10^{12}$ (**Ω**/□)) was found (Figure. S4). Therefore, scarce amount of CQDs was applied here to act as a surface/interface modifier. Due to the fact that the dimension of the CQDs is significantly smaller than the TiO_2 NPs underneath forming the ETL, the possibility of their infiltration, and their little quantities, it is difficult to resolve their presence and distribution by morphological characterization techniques such as SEM or AFM. Nevertheless, by energy-dispersive X-ray spectroscopy (EDX) elemental mapping coupled with SEM, we observed an monotonic increase of carbon atomic percentage as we increased the amount of CQD solution applied in the dynamic spin-coating (Fig. S5). Coherent

with these results, by FT-IR spectroscopy, on CQD-decorated ETL samples, the vibrational signatures attributed to CQDs are clearly visible on CQD-decorated TiO_2 ETL samples which confirm well their presence (Fig. 3(b)).

In terms of the energetics of the ETL, ultraviolet photoemission spectroscopy (UPS) experiments revealed a slight modification due to CQD decoration in terms of binding energy on both the Fermi edge region and the secondary electron cutoff region (Fig. 3(c)). The valence band maximum (VBM) of samples were calculated by $E_{VBM} = h\nu - E_{cutoff} + E_{onset}$ to be about -7.5 eV and -7.2 eV for bare TiO_2 and the CQD-decorated TiO_2 ETL sample (below termed as CQD/TiO_2), respectively. Based on the optical bandgap of the TiO_2 ETL, it can be estimated that there is a slight lifting of the conduction band minimum (CBM) of the ETL due to the CQD decoration (Fig. 3(d)), which may potentially increase the build-in potential inside the PSC which is advantageous for V_{oc}.

In terms of the surface property of the ETL, a significantly reduced contact angle (~ 8.8°) was observed on the surface of CQD/TiO_2 (Fig. 3(e)) in comparison to that observed on bare TiO_2 ETL (~ 20.2°) (Fig. 3(f)), suggesting that the CQD decoration renders the ETL surface more hydrophilic. As a result, the morphology of the perovskite film grown on top was strongly impacted, as revealed by the top-view SEM images where larger perovskite grain size was observed on the CQD/TiO_2 sample (with an average lateral dimension of ~ 872 nm) than that on bare TiO_2 ETL (~ 609 nm) (the measured grain size distribution is shown in Fig. S6). The XRD spectra measured on the perovskite thin films deposited on top also revealed slightly sharper and higher intensity on the diffraction peaks associated with the decoration of CQDs at the interface (Fig. 3(g)), which corroborates well the enlarged grain size observations by SEM. Such an enhanced perovskite crystallinity also impacts strongly on their static and time-resolved photoluminescence (TRPL) characteristics. As shown in Fig. 4(a) and 4(b), the static PL of the perovskite thin film deposited on CQD/TiO_2 exhibits a larger intensity in comparison

to that deposited on bare TiO_2 and the TRPL traces reveal a longer carrier average lifetime (651 ns *v.s.* 106 ns). This is likely due to the reduced defect-assisted nonradiative recombination associated with the larger perovskite grain size achieved on the CQD-decorated ETLs.

The device characteristics measured on completed PSCs show that a moderate amount of CQD decoration at the ETL/absorber interface can boost the photovoltaic performance. As shown in Fig. 4(c) and (d) and the tables summarizing their photovoltaic parameters (Table S2 and S3), the condition of applying 50 μL of CQDs on TiO_2 led to a ~ 3.8% increase in J_{sc} in comparison to the control sample together with a slight increase in the V_{oc} and fill-factor (FF). This may be a combined consequence of the above-discussed increased grain size of the perovskite absorber layer and the modification of the energetics of the ETL. Indeed, coherent with these observations, transient photovoltage decay (TPV) measurements reveal also slower photovoltage decay characteristics on the PSCs with an optimized CQD-decoration than the control sample. Electrochemical impedance spectroscopy (EIS) was applied to further characterize these solar cells. Fig. 4(f) shows the Nyquist plots and the equivalent circuit used for the analysis, where the R_s, R_{tr}, R_{rec}, and *CPE* represent the series resistance, the charge transfer resistance, the recombination resistance at the interface and the chemical capacitance, respectively.[13,21] Notably, a much larger R_{rec} (3.9 kΩ) in CQD-decorated solar cells was observed than the control sample (2.4 kΩ). Both TPV and EIS measurements indicate that there is less severe charge recombination in the CQD-decorated PSCs (under the current interfacial configuration II) than the control condition likely due to the increased crystallinity of the perovskite layer (and therefore reduced grain boundaries and defects) and/or the passivation of some defects sites due to the inserted CQDs. The reason of why further increasing the amount of CQDs at the interface than the optimized condition leads to J_{sc} loss remain speculative (Fig. S3). At such conditions where large amounts of CQDs were inserted at the interface, it is

possible that the benefits of achieving larger perovskite grain size is somehow off-set by the poorer charge transport and extraction at the interface.

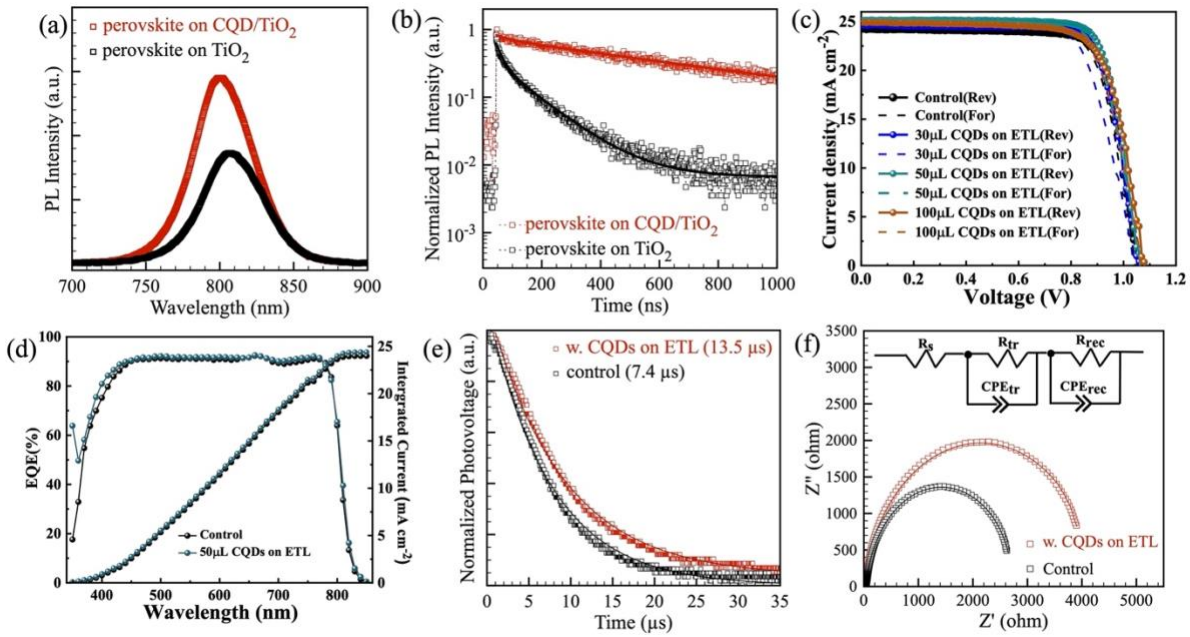

Figure 4. *(a) Steady state photoluminescence (PL) spectra and (b) TRPL traces of the perovskite thin films deposited onto a CQD-decorated TiO_2-ETL (red data) and a bare TiO_2-ETL (control, dark data) both on FTO glass substrates. (c) The J-V characteristics comparing solar cells without (control) and with different amounts of CQDs inserted at the ETL/absorber interface, measured under simulated AM1.5G solar illumination operated at 1-sun (100 mW cm^{-2}). Solid dots and lines represent the reverse scan (from V_{oc} to 0 V) and the dashed lines present the forward scan (from 0 V to V_{oc}). (d) External quantum efficiency (EQE) spectra of the optimized condition (deposited with 50 μL CQDs) displayed in (c) together with their integrated photocurrent density. (e) Transient photovoltage decay (TPV) curves with the average decay time indicated in brackets and the (f) Nyquist plots (measured by EIS under a forward bias at Voc in dark) on the solar cells without and with the optimized amount of CQDs decorated at the ETL/absorber interface. Empty squares are the measured data and the solid lines represent the fits.*

2.3. Configuration III: Combining exterior and interfacial modifications to enhance both efficiency and stability

In this section, by a synergetic combination of both configuration I and II, exterior and interfacial application of CQDs, we demonstrate a simple route to maximized the PSC stability

against UV illumination without any scarification on their photovoltaic efficiencies. Such a combination is rationalized by the fact that, while the optimized CQD layer in configuration I can screen and downshift UV photons and thus impacting the solar cells' stability against UV, the J_{sc} of the PSCs was somehow reduced due to optical loss. In comparison, the UV screening and LDS property of the optimized amount of CQDs applied in configuration II as a interfacial modifier is modest (due to their limited quantities) but the better crystallinity of the perovskite layer grown on top results in improvements in J_{sc} and less severe charge recombination. The combination of both configurations (termed as configuration III, Fig. 5(a)), thus represents a bright route to optimize both the solar cells' efficiency and stability against UV. The *J-V* characteristics under 1-sun AM1.5G illumination, the corresponding EQE spectrum, and the stabilized PCEs by maximum power point (MPP) tracking were measured on the optimized PSC with CQDs applied in configuration III and on the control device (without CQDs) (Figure 5(b), (c) and (d)). The statistics allowing a cross-comparison on the photovoltaic parameters of the different PSCs with and without CQDs under different configurations fabricated in this work are summarized in **Table 1**. Notably, the best (and averaged) PCE obtained from *J-V* tests under 1-sun illumination of the control device and the PSCs with CQDs in configuration III is 20.01 % (19.56 ± 0.76 %) and 20.39 % (19.88 ± 0.32 %), respectively, indicating no scarification (with even a slight improvement) on the different photovoltaic parameters due to the application of CQDs in configuration III. While FAMA-based PSCs with a similar *n-i-p* device architecture as the present study can achieve high PCEs (~23% to 25.6%) by various transport-layer-engineering, additives, interfacial passivation, and additive/passivation-combined approaches, the "control" or reference PSCs (without these approaches) reported in previous studies typically exhibited a PCE in the range from 20% to 23% (summarized in Table S4 in comparison to the present study),[62–68] which further depends on the device area and was found to be highly sensitive to fabrication conditions.[69–71] We strengthen that the main focus

of the present study is to present an effective bottom-up approach, leading to no PCE scarification, to act against the notorious UV-induced PSC degradation that will be discussed below.

Figure 5(e) exhibits the cross-comparison of the device stability measured in ambient air at room temperature (~ 25 °C) under continuous UV illumination (at λ = 365 nm, 5 mW cm^{-2}) of the different unencapsulated PSCs without CQDs (the control samples), with CQDs applied in the above-mentioned three different configurations, and with a commercial UV filter ($\lambda_{cut\text{-}on}$ = 400 nm). Each of these curves exhibits the average degradation behavior measured on three PSCs of the same type fabricated and degraded under identical conditions. The PSCs under the control condition (without CQDs and without any UV filter) degraded rather rapidly, losing ~ 20% of their PCEs only after 5 hours of continuous UV illumination and exhibiting only ~ 40% their initial PCE after 47 hours of illumination (the black curve in Fig. 5(e)). XRD experiments were carried out on them before and after degradation. As shown in Fig. 5(f), on the control devices, after degradation, there were new diffraction peaks appearing which can be assigned to the δ-phase of $FAPbI_3$. This indicates that the exposure of the current PSCs under continuous UV illumination in air led to perovskite decomposition and the generation of the photovoltaic-inactive δ-phase. Thanks to the strong UV absorption of the CQD optical layer, this degradation behavior was significantly slowed down on the PSCs with their front sides covered by CQDs (red curve, Fig. 5(f)). Indeed, with the application of CQDs, different degrees of improvements in terms of stability were achieved: For configuration II (interfacial decoration), a modest improvement on device stability was observed (the blue curve of Fig. 5(d)), exhibiting a PCE loss of < 10 % and ~ 32 % after 5 and 100 hours of degradation under UV illumination, respectively. In comparison, CQDs applied in configuration I, configuration III, and a commercial UV filter all allow for a remarkable enhancement on the device stability against UV (Fig. 5(e), and a zoom-in view in Fig. S7). In comparison to that observed on the control

sample, all these three curves exhibit a very similar degradation behavior over time, with a much slower PCE loss of < 2 % after 5 hours and < 6 % after 100 hours of degradation in air under continuous UV illumination. In contrast to the PSCs with a commercial UV filter or those with CQDs applied in configuration I, where the benefits of UV stability is somehow offset by photovoltaic performance loss, the unique advantages of CQDs applied in the synergetic configuration III thus lead to a large degradation improvement against UV as shown in Fig. 5(e) without any scarification on the J_{sc} and the PCE of the devices (Table 1).

Besides continuous UV illumination, on the most optimized condition (with CQDs applied in configuration III) and on the control device, the device degradation behavior under continuous 1-sun (AM1.5G) illumination was measured at room temperature in argon (Figure 5(g)). Significant stability improvement was observed on the PSCs with CQDs applied, capable to maintain > 94 % of their initial PCEs after 100h of degradation in comparison to the control devices which maintains only about 60% of their initial PCEs under identical degradation conditions). These observation is likely a combined consequence of the UV-screening characteristics of CQDs and the improved perovskite crystallinity due to the application of CQDs as interfacial modifiers.

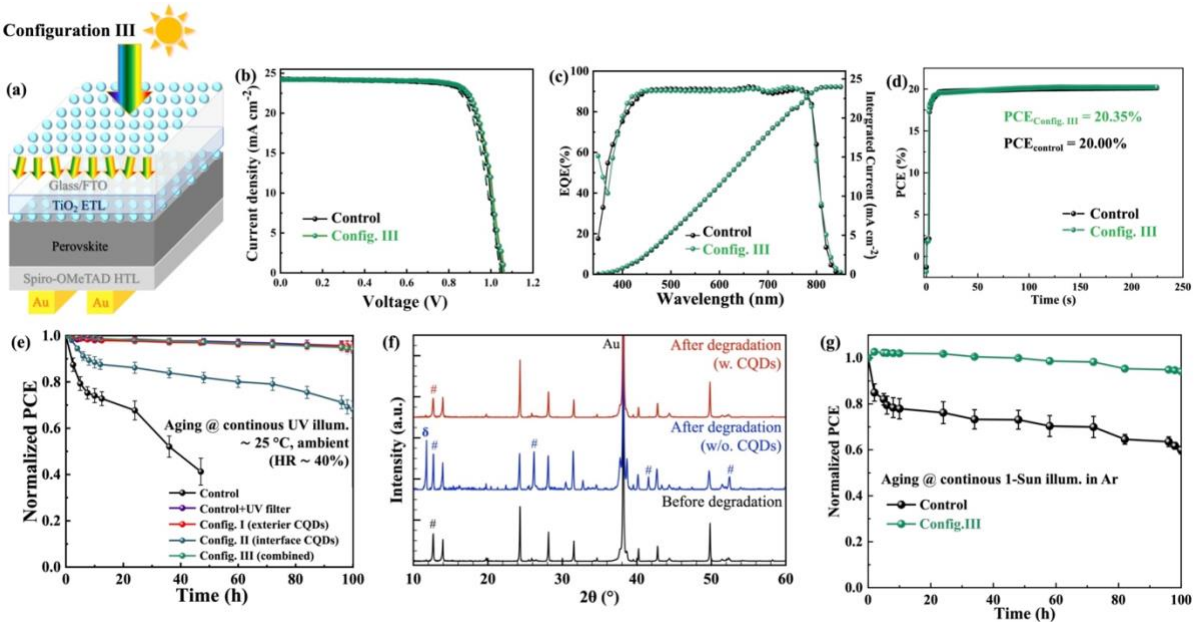

Figure 5. *(a) Schematic of configuration III combining the optimized conditions of both configuration I and II. (b) The J-V characteristics measured under simulated AM1.5G 1-Sun illumination (100 mW cm^{-2}), (c) the corresponding EQE spectra, and (d) maximum power point (MPP) MPP tracking under 1-sun AM1.5G illumination of a control device (w/o. CQDs) and a solar cell applying CQDs according to the configuration III described in (a). (e) The evolution of the PCE over time on unencapsulated devices kept under continuous UV illumination (λ = 365 nm, 5 mW cm^{-2}) measured in air at ~25 °C. Different PSCs, without and with CQDs applied in different configurations, are compared together with the solar cells applied with a commercial UV filter (λ_{cut-on} = 400 nm). (f) XRD spectra measured on the completed PSCs before (black) and after aging with (red) and without (blue) CQDs applied as a UV LDS layer. The "#" and the "δ" symbol label the diffraction peaks assigned to PbI_2 and the δ-phase of $FAPbI_3$, respectively. (g) The evolution of the PCE over time on unencapsulated devices kept under continuous 1-sun AM1.5G illumination (100 mW cm^{-2}) measured in argon at room temperature (~25 °C).*

Table 1. Summary of the average photovoltaic parameters measured on PSCs without ("control" sample) and with CQDs deposited under different configurations in comparison with the solar cells with a commercial UV filter (λ_{cut-on} = 400 nm) placed in their front side. J_{sc} = short-circuit current density; V_{oc} = open-circuit voltage; *FF* = fill factor; *PCE* = power conversion efficiency.

Solar cells	J_{sc} **(mA cm^2)**	V_{oc} **(V)**	***FF*** **(%)**	***PCE*** **(%)**
Control (w./o. CQDs)	24.13 ± 0.48	1.06 ± 0.02	76.43 ±1.79	19.56 ± 0.76
w. UV filter	22.05 ± 0.45	1.06 ± 0.01	72.33 ± 0.92	17.12 ± 0.49
Configuration I	22.52 ± 0.46	1.05 ± 0.02	74.81 ± 1.74	17.64 ± 0.70
Configuration II	24.74 ± 0.66	1.07 ± 0.01	77.08 ± 1.25	20.40 ± 0.40
Configuration III	24.21 ± 0.50	1.06 ± 0.01	76.80 ± 1.21	19.88 ± 0.32

Finally, in order to demonstrate the generality of the current method based on CQDs, we further applied CQDs under the optimized configuration III on solar cells with another perovskite composition, triple-cation and mixed halide perovskite of $Cs_{0.05}(FA_{0.83}MA_{0.17})_{0.95}Pb(I_{0.83}Br_{0.17})_3$. As shown in Figure S8, after 100h of continuous degradation in air under UV illumination, similar stability improvement was also observed on these triple-cation PSCs thanks to CQDs. These results suggest that the effectiveness of the current method based on CQDs is not restrictive to the perovskite compositions applied but can be extended to other compositions.

3. Conclusions

In summary, on PSCs based on $FA_{1-x}MA_xPbI_3$, we demonstrated a new approach to enhance the solar cell stability against the notorious UV photons without scarification on device efficiency. This approach, based on the application of solution-processed bottom-up synthesized colloidal CQDs, harvests both the unique optical and structural/surface properties of the CQDs. Thorough optimizations were carried out in terms of the different amounts of the CQDs and the different location/interfaces of the solar cells where they are applied. Similar to that achieved by a commercial UV filter, the CQD optical layer deposited on the solar cell exterior front-side (configuration I) can lead to a significant stability improvement against UV illumination but with a cost of J_{sc} (and therefore PCE) due to optical loss. The CQDs inserted at the ETL/absorber interface (configuration II) improved the interfacial property and led to more crystalline perovskite layer with larger grain sizes, resulting in higher PCEs and reduction of charge recombination. But, under this configuration, the device stability enhancement

against UV was modest due to the limited amount of CQDs possibly be inserted before the deterioration of charge extraction. Finally, a synergetic application of CQDs (configuration III) combining both the optimized conditions achieved in configuration I and II demonstrated both efficient and robust PSCs capable to maintain > 94% of their initial PCEs after 100 hours of continuous UV illumination (λ = 365 nm, 5 mW cm^{-2}) measured in ambient air. Our study provides new insights on how both the optical and structural/surface properties of CQDs can be harvested to the maximum extent to improve both the efficiency and the stability of PSCs. Given the unique characteristics of CQDs (in terms of low-cost aqueous synthesis, the bio-sourceable precursors, and earth abundant compositions) and the effective results achieved on PSCs based on different perovskite compositions, the present synergetic strategy based on CQDs exhibit bright potentials contributing to the large-scale development of efficient and robust PSCs.

4. Experimental section

4.1. Materials

Titanium (IV) isopropoxide was purchased from Merck. Lead iodide (PbI_2, 99.999%), transparent titania (TiO_2) paste (Greatcell Solar®), formamidinium acetate (99%), methylamine solution (40 wt% in water), hydriodic acid solution (57 wt% in water), hydrobromic acid solution (47 wt% in water), N^2,N^2,$N^{2'}$,$N^{2'}$,N^7,N^7,$N^{7'}$,$N^{7'}$-octakis(4-methoxyphenyl)-9,9′-spirobi[9*H*-fluorene]-2,2′,7,7′-tetramine (Spiro-OMeTAD, 99%), bis(trifluoroethane)sulfonimide lithium salt (Li-TFSI, 99.95%), tris(2-(1*H*-pyrazol-1-yl)-4-*tert*-butylpyridine)cobalt(III)tri[bis(trifluoromethane)sulfonimide] (FK209, 98%), anhydrous dimethyl sulfoxide (DMSO, 99.9%), anhydrous *N*,*N*-dimethylformamide (DMF, 99.8%), anhydrous 2-propanol (IPA, 99.5%), 4-*tert*-butylpyridine (98%), anhydrous chlorobenzene (CBZ, 99.8%), anhydrous acetonitrile (99.8%), and fluorine doped tin oxide (FTO) coated glass

substrates with a sheet resistance of 13 Ω·sq were received from Sigma-Aldrich. All the chemicals were used as received without further treatment. Formamidinium iodide (FAI), methylammonium iodide (MAI) and methylammonium chloride (MACl) were synthesized respectively by reacting formamidinium acetate with hydroiodic acid (for FAI), or methylamine solution with hydroiodic acid (for MAI) or hydrochloric acid (for MACl) according to a previous reported protocol.[72]

4.2. Preparation of carbon quantum dots (CQDs)

Carbon quantum dots solution was prepared according to a method previously described.[37] Typically, citric acid (1.0501 g) and ethylenediamine (335 μL) was first dissolved in 10 mL of deionized (DI) water. The solution was then sealed in a 50-mL-volumn poly(tetrafluoroethylene) (Teflon)-lined autoclave and kept into an oven at 150ºC for five hours. After five hours, the autoclave was allowed to cool down to room temperature naturally. The resultant product, a light brown liquid containing CQDs, was then purified by dialysis in DI water for 24 hours. In a typical synthesis, after dialysis, 18 mL of CQD solution in DI-water was obtained (which corresponds to an optical density (O.D.) of 1.96 at λ = 350 nm measured by UV-Visible optical absorbance (with a 1-cm optical path cuvette) and a mass concentration of ~ 11 mg/mL). This CQD water solution was then applied directly in the device fabrication procedures described below.

4.3. Fabrication of $FA_{1-x}MA_xPbI_3$ and $Cs_{0.05}(FA_{0.83}MA_{0.17})_{0.95}Pb(I_{0.83}Br_{0.17})_3$ PSCs

FTO-coated glass substrates were cleaned sequentially by ultrasonic baths of detergent (2% of Hellmanex III), DI-water, acetone, and isopropyl alcohol for 15 minutes each. After blow-drying with compressed air, these substrates were further treated by a UV/Ozone for 20 minutes. In order to prepare the compact TiO_2 (cp-TiO_2) layer, a sol-gel precursor solution was prepared by mixing 0.675 mL of titanium isopropoxide, 17.75 mL of IPA, and 0.25 g of diethanolamine under magnetic stirring at room temperature for 10 minutes, followed by adding 17.5 μL of DI-

water and overnight stirring. This solution was then spin-coated (4000 rpm for 30s) onto cleaned FTO substrates which were subsequently heat-treated first by a hotplate in air at 125 °C for 10 minutes and then in a muffle furnace at 450°C for 1 hour resulting a cp-TiO_2 layer on FTO. Separately, in order to prepare the mesoporous TiO_2 layer, transparent titania paste was diluted by ethanol with a weight ratio of 1:10 with a 12-hour stirring. Then 40 µL of this solution was spin-coated (at 3000 rpm, 30s) onto the above-mentioned cp-TiO_2/FTO substrates, followed by drying on a hotplate at 125 °C for 10 minutes and then annealing in a muffle furnace at 510 °C for 30 minutes. For PSCs based on $FA_{1-x}MA_xPbI_3$ (x = 0.1), the perovskite layer was deposited by two-steps method according to the literatures.[67,73,74] Typically, in a N_2-filled glovebox, a solution containing 1.5 M of PbI_2 in anhydrous DMF: DMSO (9:1, v/v) was spin-coated onto the above-mentioned FTO/cp-TiO_2/mp-TiO_2 substrates at 1500 rpm for 30 s followed by a heat-treatment at 70 °C on a hotplate for 1 minute. After cooling to room temperature, another solution containing a mixture of FAI: MAI: MACl (90 mg: 9 mg: 9 mg) in 1 mL IPA was spin-coated onto these PbI_2 films (2000 rpm, 30 seconds) followed by heating on a hotplate at 150 °C for 15 minutes before cooling down to room temperature. For PSCs based on $Cs_{0.05}(FA_{0.83}MA_{0.17})_{0.95}Pb(I_{0.83}Br_{0.17})_3$, the fabrication procedure was identical to the procedure reported in our previous work.[75] The hole transport layer was deposited by spin-coating (4000 rpm for 30s) a solution, which was prepared in advance by dissolving 72.3 mg of spiro-OMeTAD, 28.8 µL of 4-tert-butylpyridine, 17.5 µL of Li-TFSI solution (520 mg/mL in acetonitrile) and 12 µL of FK209 (376 mg/mL in acetonitrile) in 1 mL chlorobenzene. Finally, 80-nm-thick back contact electrodes of gold were thermally evaporated (with a base pressure of ~10^{-6} mbar) through a shadow mask onto the stack to complete the solar cell fabrication, defining the device active area as 0.1 cm^2. Concerning the optical layer based on CQDs applied in the exterior of the device (configuration I), the device fabrication procedure was the same as that mentioned above except that, before depositing the perovskite absorber, in air, on the front

(glass) side of clean glass/FTO/cp-TiO_2/mp-TiO_2 substrates, different volumes (50 µL, 100 µL, and 200 µL) of CQDs solution were applied by drop-casting followed by a heating on a hotplate at 100 °C for 10 minutes leading to the different thickness of the CQD films achieved. Concerning the interfacial modification approach by CQDs at the TiO_2/perovskite interface (configuration II), the device fabrication procedure was the same as mentioned above except that, before perovskite deposition, in air, on the surface the mp-TiO_2 ETL layer, different volumes of CQDs solution were deposited by dynamic spin-coating (at 3000 rpm for 30 s) followed by a mild heat-treatment at 100 °C for 10 min on a hot plate. Concerning configuration III (the combined treatments), the above-mentioned CQD deposition procedures of configuration I and II were applied together on the same PSC.

4.4. Materials and optical characterizations

SEM and EDX elemental mapping experiments were performed by a FEI Magellan 400 system equipped with a standard field emission gun source. TEM characterizations were performed by a JEOL 2010 TEM microscope operated at 200 kV. XRD spectra were obtained by a PANalytical X'Pert X-ray diffractometer using Cu-Kα radiation. UV-visible absorption spectra were recorded by a JASCO V770 UV-Vis-NIR spectrometer. FT-IR spectroscopy was measured by Perkin-Elmer Spectrum Two instrument in an attenuated total reflection (ATR) infrared mode. Static PL experiments was carried out under a fiber-coupled LED excitation (at λ = 365 nm) and the PL was recorded in a reflection mode by an optical fiber connected with a computer-controlled Ocean optics HR4000 spectrometer. PL imaging was achieved by a home-build microscopy setup where a modulated laser excitation (λ = 405 nm) was focused at a 1-µm spot on the sample, the position of which was controlled by a motorized stage. On each sample spot, the PL was recorded by a lock-in technique by a photomultiplier tube (PMT) detector from a 40-nm-wavelength window centered at λ = 536 nm. For time-resolved PL experiments, the samples were excited by a picosecond laser diode (Alphalas) operating at

405 nm with PL detected by a Si single-photon avalanche diode (Micro Photon Devices Italy). This picosecond laser supplied a trigger signal to a computer-controlled PicoHarp 300 TCSPC module from which the histograms of photon arrival times were obtained.

Contact angle experiments were measured by a computer-controlled Ossila contact angle goniometer. UPS was performed using at room temperature, in an ultra-high vacuum chamber ($< 2\times10^{-10}$ mbar) with photon energy of 21.2eV using a He discharge light source.

4.5. Photovoltaic characterizations

The photocurrent density-voltage (*J-V*) characteristic curves were measured at room temperature (25 °C) in an N_2-filled glovebox by a computer controlled Keithley 2612B source measurement unit (SMU). Solar cells were illuminated from the transparent glass/FTO substrate (front) side by a class ABB (ASTM E927-10) Newport LCS-100 solar simulator with an AM 1.5G filter operated under 1-sun conditions (at 100 mW cm^{-2}). The 1-Sun light intensity was measured by a calibrated Si reference solar cell (ReRa Solutions B.V.). External quantum efficiency (EQE) measurements were performed in air at 25°C. Specifically, a monochromatic light beam was obtained from a white light source coupled with an Oriel Cornerstone monochromator and appropriate order sorting filters. The monochromatic illumination was calibrated by a NIST-calibrated Si photodiode. The solar cell short circuit current (I_{sc}) under each monochromatic wavelength was measured by a Keithley 2634B SMU. The EQE spectrum was then determined by $\mathrm{EQE}(\%) = \frac{J_{sc}(\mathrm{A}\,cm^{-2})}{\mathrm{P}(\mathrm{W}\,cm^{-2})} \times \frac{1240}{\lambda(\mathrm{nm})} \times 100$ where P (W cm^{-2}) is the power density of the monochromatic illumination and J_{sc} (A cm^{-2}) is the measured short circuit current density under each monochromatic wavelength. For transient photovoltage measurements, which were carried out under ambient conditions at 25 °C, an ABET solar simulator together with a neutral density filter supplied a static white light background (at 0.14-Sun intensity) for the solar cells under test. In addition to the white light background, the solar cells were illuminated by laser pulses with a rise and fall time less than 100 ns achieved by modulating a

continuous wave green laser (λ = 520 nm, StingRay from Coherent) with a function generator (AIM-TTI Instruments, TG1006). The achieved transient photovoltage was amplified by the Stanford Research systems SR560 low-noise voltage preamplifier with an input impedance of 100 MΩ and then recorded by a Tektronix digital oscilloscope (DPO2024B) with input impedance of 1 MΩ. The electrochemical impedance spectroscopy (EIS) measurements were carried out by a computer-controlled electrochemical workstation (Agilent, E4980A) in a N_2-filled glovebox on solar cells kept in dark, with a frequency ranging from 20 Hz to 2 MHz, a modulation amplitude of 20 mV, and an external applied bias holding near the open-circuit voltage of the solar cell. Concerning the measurements of the solar cell degradation behavior against UV, unencapsulated devices under test were illuminated continuously by a UV lamp (λ = 365nm, power density calibrated as 5 mW/cm^2) at room temperature (25 °C) in ambient air (relative humidity about 40%). Concerning the measurements of the solar cell degradation behavior under continuous 1-sun (AM1.5G) illumination, unencapsulated devices under test were illuminated continuously at room temperature (25 °C) in an Ar-filled glovebox.

Acknowledgements

D. Zhang received PhD thesis funding from the China Scholarship Council. Z. Chen, L. Aigouy, and L. Billot acknowledge the PEPR TASE "MINOTAURE" project (ANR-22-PETA-0015) and the CNRS for supports.

Conflict of Interest

The authors declare no conflict of interest.

5. References

[1] K. P. Goetz, A. D. Taylor, Y. J. Hofstetter, Y. Vaynzof, *ACS Appl Mater Interfaces* **2021**, *13*, 1.

[2] M. V. Khenkin, E. A. Katz, A. Abate, G. Bardizza, J. J. Berry, C. Brabec, F. Brunetti, V. Bulović, Q. Burlingame, A. Di Carlo, R. Cheacharoen, Y.-B. Cheng, A. Colsmann, S. Cros, K. Domanski, M. Dusza, C. J. Fell, S. R. Forrest, Y. Galagan, D. Di Girolamo, M. Grätzel, A. Hagfeldt, E. von Hauff, H. Hoppe, J. Kettle, H. Köbler, M. S. Leite, S. Liu, Y.-L. Loo, J. M. Luther, C.-Q. Ma, M. Madsen, M. Manceau, M. Matheron, M. McGehee, R. Meitzner, M. K. Nazeeruddin, A. F. Nogueira, Ç. Odabaşı, A. Osherov, N.-G. Park, M. O. Reese, F. De Rossi, M. Saliba, U. S. Schubert, H. J. Snaith, S. D. Stranks, W. Tress, P. A. Troshin, V. Turkovic, S. Veenstra, I. Visoly-Fisher, A. Walsh, T. Watson, H. Xie, R. Yıldırım, S. M. Zakeeruddin, K. Zhu, M. Lira-Cantu, *Nat Energy* **2020**, *5*, 35.

[3] J.-P. Correa-Baena, M. Saliba, T. Buonassisi, M. Grätzel, A. Abate, W. Tress, A. Hagfeldt, *Science (1979)* **2017**, *358*, 739.

[4] S. D. Stranks, G. E. Eperon, G. Grancini, C. Menelaou, M. J. P. Alcocer, T. Leijtens, L. M. Herz, A. Petrozza, H. J. Snaith, *Science (1979)* **2013**, *342*, 341.

[5] S. G. Motti, D. Meggiolaro, S. Martani, R. Sorrentino, A. J. Barker, F. De Angelis, A. Petrozza, *Advanced Materials* **2019**, *31*, 1901183.

[6] Y. Tu, J. Wu, G. Xu, X. Yang, R. Cai, Q. Gong, R. Zhu, W. Huang, *Advanced Materials* **2021**, *33*, 2006545.

[7] S. S. Dipta, A. Uddin, *Energy Technology* **2021**, *9*, 2100560.

[8] T. Chen, J. Xie, P. Gao, *Advanced Energy and Sustainability Research* **2022**, *3*, 2100218.

[9] M. Zayat, P. Garcia-Parejo, D. Levy, *Chem Soc Rev* **2007**, *36*, 1270.

[10] S. Ito, S. Tanaka, K. Manabe, H. Nishino, *The Journal of Physical Chemistry C* **2014**, *118*, 16995.

[11] T. Leijtens, G. E. Eperon, S. Pathak, A. Abate, M. M. Lee, H. J. Snaith, *Nat Commun* **2013**, *4*, 2885.

[12] A. Farooq, M. R. Khan, T. Abzieher, A. Voigt, D. C. Lupascu, U. Lemmer, B. S. Richards, U. W. Paetzold, *ACS Appl Energy Mater* **2021**, *4*, 3083.

[13] H. Xu, Y. Miao, N. Wei, H. Chen, Z. Qin, X. Liu, X. Wang, Y. Qi, T. Zhang, Y. Zhao, *Adv Energy Mater* **2022**, *12*, 2103151.

[14] M. Degani, Q. An, M. Albaladejo-Siguan, Y. J. Hofstetter, C. Cho, F. Paulus, G. Grancini, Y. Vaynzof, *Sci Adv* **2024**, *7*, eabj7930.

[15] J. B. Patel, P. Tiwana, N. Seidler, G. E. Morse, O. R. Lozman, M. B. Johnston, L. M. Herz, *ACS Appl Mater Interfaces* **2019**, *11*, 21543.

[16] T. Trupke, M. A. Green, P. Würfel, *J Appl Phys* **2002**, *92*, 1668.

[17] J. Cui, P. Li, Z. Chen, K. Cao, D. Li, J. Han, Y. Shen, M. Peng, Y. Q. Fu, M. Wang, *Appl Phys Lett* **2016**, *109*, 171103.

[18] F. Bella, G. Griffini, J. P. Correa-Baena, G. Saracco, M. Grätzel, A. Hagfeldt, S. Turri, C. Gerbaldi, *Science (1979)* **2016**, *354*, 203.

[19] N. Chander, A. F. Khan, P. S. Chandrasekhar, E. Thouti, S. K. Swami, V. Dutta, V. K. Komarala, *Appl Phys Lett* **2014**, *105*, 033904.

[20] P. Chen, Z. Wang, S. Wang, M. Lyu, M. Hao, M. Ghasemi, M. Xiao, J.-H. Yun, Y. Bai, L. Wang, *Nano Energy* **2020**, *69*, 104392.

[21] Q. Guo, J. Wu, Y. Yang, X. Liu, W. Sun, Y. Wei, Z. Lan, J. Lin, M. Huang, H. Chen, Y. Huang, *Nano Energy* **2020**, *77*, 105183.

[22] H.-S. Roh, G. S. Han, S. Lee, S. Kim, S. Choi, C. Yoon, J.-K. Lee, *J Power Sources* **2018**, *389*, 135.
[23] C. Chen, H. Li, J. Jin, X. Chen, Y. Cheng, Y. Zheng, D. Liu, L. Xu, H. Song, Q. Dai, *Adv Energy Mater* **2017**, *7*, 1700758.
[24] S. S. Shin, E. J. Yeom, W. S. Yang, S. Hur, M. G. Kim, J. Im, J. Seo, J. H. Noh, S. Il Seok, *Science (1979)* **2017**, *356*, 167.
[25] T.-P. Chen, C.-W. Lin, S.-S. Li, Y.-H. Tsai, C.-Y. Wen, W. J. Lin, F.-M. Hsiao, Y.-P. Chiu, K. Tsukagoshi, M. Osada, T. Sasaki, C.-W. Chen, *Adv Energy Mater* **2018**, *8*, 1701722.
[26] H. Zhang, H. Wang, H. Zhu, C. Chueh, W. Chen, S. Yang, A. K. -Y. Jen, *Adv Energy Mater* **2018**, *8*, 1702762.
[27] Y. Sun, X. Fang, Z. Ma, L. Xu, Y. Lu, Q. Yu, N. Yuan, J. Ding, *J Mater Chem C Mater* **2017**, *5*, 8682.
[28] W. Li, J. Li, G. Niu, L. Wang, *J Mater Chem A Mater* **2016**, *4*, 11688.
[29] W. Li, W. Zhang, S. Van Reenen, R. J. Sutton, J. Fan, A. A. Haghighirad, M. B. Johnston, L. Wang, H. J. Snaith, *Energy Environ Sci* **2016**, *9*, 490.
[30] X. Deng, Z. Cao, C. Li, S. Wang, F. Hao, *Journal of Energy Chemistry* **2022**, *65*, 592.
[31] C. J. Reckmeier, J. Schneider, A. S. Susha, A. L. Rogach, *Opt Express* **2016**, *24*, A312.
[32] Y. Vyas, P. Chundawat, D. Dharmendra, P. B. Punjabi, C. Ameta, *Int J Hydrogen Energy* **2021**, *46*, 37208.
[33] L. Cao, K. A. Shiral Fernando, W. Liang, A. Seilkop, L. Monica Veca, Y.-P. Sun, C. E. Bunker, *J Appl Phys* **2019**, *125*, 220903.
[34] G. Yang, C. Wu, X. Luo, X. Liu, Y. Gao, P. Wu, C. Cai, S. S. Saavedra, *The Journal of Physical Chemistry C* **2018**, *122*, 6483.
[35] J. Liu, R. Li, B. Yang, *ACS Cent Sci* **2020**, *6*, 2179.
[36] S. Zhu, Q. Meng, L. Wang, J. Zhang, Y. Song, H. Jin, K. Zhang, H. Sun, H. Wang, B. Yang, *Angewandte Chemie - International Edition* **2013**, *52*, 3953.
[37] M. Chaudhary, C. Xin, Z. Hu, D. Zhang, G. Radtke, X. Xu, L. Billot, C. Tripon-Canseliet, Z. Chen, *Adv Electron Mater* **2023**, *9*, 2300159.
[38] X. Hu, Y. Li, Y. Xu, Z. Gan, X. Zou, J. Shi, X. Huang, Z. Li, Y. Li, *Food Chem* **2021**, *339*, 127775.
[39] Y. Vyas, P. Chundawat, D. Dharmendra, A. Jain, P. B. Punjabi, C. Ameta, *Mater Chem Phys* **2022**, *281*, 125921.
[40] Y. Vyas, P. Chundawat, Dharmendra, P. B. Punjabi, C. Ameta, *ChemistrySelect* **2021**, *6*, 8566.
[41] M. Ali, R. Riaz, S. Bae, H.-S. Lee, S. H. Jeong, M. J. Ko, *ACS Appl Mater Interfaces* **2020**, *12*, 10369.
[42] D. Dai, X. Tu, X. Li, T. Lv, F. Han, *Progress in Photovoltaics: Research and Applications* **2019**, *27*, 283.
[43] R. Riaz, M. Ali, T. Maiyalagan, A. S. Anjum, S. Lee, M. J. Ko, S. H. Jeong, *Appl Surf Sci* **2019**, *483*, 425.
[44] H. Bian, Q. Wang, S. Yang, C. Yan, H. Wang, L. Liang, Z. Jin, G. Wang, S. (Frank) Liu, *J Mater Chem A Mater* **2019**, *7*, 5740.
[45] A. A. Maxim, S. N. Sadyk, D. Aidarkhanov, C. Surya, A. Ng, Y.-H. Hwang, T. Sh. Atabaev, A. N. Jumabekov, *Nanomaterials* **2020**, *10*, 291.
[46] A. A. Maxim, D. Aidarkhanov, T. Sh. Atabaev, A. N. Jumabekov, A. Ng, *Mater Today Proc* **2022**, *49*, 2487.
[47] J. Jin, C. Chen, H. Li, Y. Cheng, L. Xu, B. Dong, H. Song, Q. Dai, *ACS Appl Mater Interfaces* **2017**, *9*, 14518.
[48] C. Marionnet, C. Tricaud, F. Bernerd, *Int J Mol Sci* **2014**, *16*, 68.

[49] D. Benetti, E. Jokar, C.-H. Yu, A. Fathi, H. Zhao, A. Vomiero, E. Wei-Guang Diau, F. Rosei, *Nano Energy* **2019**, *62*, 781.
[50] Y. Ma, H. Zhang, Y. Zhang, R. Hu, M. Jiang, R. Zhang, H. Lv, J. Tian, L. Chu, J. Zhang, Q. Xue, H.-L. Yip, R. Xia, X. Li, W. Huang, *ACS Appl Mater Interfaces* **2019**, *11*, 3044.
[51] Q. Guo, F. Yuan, B. Zhang, S. Zhou, J. Zhang, Y. Bai, L. Fan, T. Hayat, A. Alsaedi, Z. Tan, *Nanoscale* **2019**, *11*, 115.
[52] S. Li, Y. Li, K. Liu, M. Chen, W. Peng, Y. Yang, X. Li, *J Colloid Interface Sci* **2021**, *600*, 691.
[53] Y. Wang, J. Zhang, S. Chen, H. Zhang, L. Li, Z. Fu, *J Mater Sci* **2018**, *53*, 9180.
[54] Y. Wen, G. Zhu, Y. Shao, *J Mater Sci* **2020**, *55*, 2937.
[55] X. Zhu, J. Sun, S. Yuan, N. Li, Z. Qiu, J. Jia, Y. Liu, J. Dong, P. Lv, B. Cao, *New Journal of Chemistry* **2019**, *43*, 7130.
[56] W. Hui, Y. Yang, Q. Xu, H. Gu, S. Feng, Z. Su, M. Zhang, J. Wang, X. Li, J. Fang, F. Xia, Y. Xia, Y. Chen, X. Gao, W. Huang, *Advanced Materials* **2020**, *32*, 1906374.
[57] J. Liu, Y. Yin, B. He, P. Wang, M. Wang, W. Cai, Y. Han, Z. Su, J. Guo, R. Cai, S. Jin, X. Gao, J. Bian, Y. Shi, *Materials Today Physics* **2023**, *33*, 101041.
[58] H. Li, W. Shi, W. Huang, E.-P. Yao, J. Han, Z. Chen, S. Liu, Y. Shen, M. Wang, Y. Yang, *Nano Lett* **2017**, *17*, 2328.
[59] J. Liu, Q. Dong, M. Wang, H. Ma, M. Pei, J. Bian, Y. Shi, *ACS Appl Mater Interfaces* **2021**, *13*, 56265.
[60] J. K. Kim, D. N. Nguyen, J.-H. Lee, S. Kang, Y. Kim, S.-S. Kim, H.-K. Kim, *J Alloys Compd* **2020**, *818*, 152887.
[61] H. Zou, D. Guo, B. He, J. Yu, K. Fan, *Appl Surf Sci* **2018**, *430*, 625.
[62] T. Yang, W. Zhao, Y. Yang, W. Huang, K. Zhao, S. (Frank) Liu, *Advanced Materials* **2023**, *35*, 2211006.
[63] S. Zhan, Y. Duan, Z. Liu, L. Yang, K. He, Y. Che, W. Zhao, Y. Han, S. Yang, G. Zhao, N. Yuan, J. Ding, S. (Frank) Liu, *Adv Energy Mater* **2022**, *12*, 2200867.
[64] R. Sun, Q. Tian, M. Li, H. Wang, J. Chang, W. Xu, Z. Li, Y. Pan, F. Wang, T. Qin, *Adv Funct Mater* **2023**, *33*, 2210071.
[65] X. Zhu, S. Yang, Y. Cao, L. Duan, M. Du, J. Feng, Y. Jiao, X. Jiang, Y. Sun, H. Wang, S. Zuo, Y. Liu, S. (Frank) Liu, *Adv Energy Mater* **2022**, *12*, 2103491.
[66] J. Jeong, M. Kim, J. Seo, H. Lu, P. Ahlawat, A. Mishra, Y. Yang, M. A. Hope, F. T. Eickemeyer, M. Kim, Y. J. Yoon, I. W. Choi, B. P. Darwich, S. J. Choi, Y. Jo, J. H. Lee, B. Walker, S. M. Zakeeruddin, L. Emsley, U. Rothlisberger, A. Hagfeldt, D. S. Kim, M. Grätzel, J. Y. Kim, *Nature* **2021**, *592*, 381.
[67] P. Wang, R. Li, B. Chen, F. Hou, J. Zhang, Y. Zhao, X. Zhang, *Advanced Materials* **2020**, *32*, 1905766.
[68] Q. Jiang, Y. Zhao, X. Zhang, X. Yang, Y. Chen, Z. Chu, Q. Ye, X. Li, Z. Yin, J. You, *Nat Photonics* **2019**, *13*, 460.
[69] J. Ye, G. Liu, L. Jiang, H. Zheng, L. Zhu, X. Zhang, H. Wang, X. Pan, S. Dai, *Appl Surf Sci* **2017**, *407*, 427.
[70] M. Saliba, J.-P. Correa-Baena, C. M. Wolff, M. Stolterfoht, N. Phung, S. Albrecht, D. Neher, A. Abate, *Chemistry of Materials* **2018**, *30*, 4193.
[71] Y. Fang, T. Tian, M. Yang, Y. Tan, J.-X. Zhong, Y. Huang, X. Wang, J. Tao, S. Yang, C. Zou, S. Yang, Y. Peng, Q. Xue, W.-Q. Wu, *Adv Funct Mater* **2023**, *33*, 2303674.
[72] Z. Hu, H. Xiang, M. Schoenauer Sebag, L. Billot, L. Aigouy, Z. Chen, *Chemical Communications* **2018**, *54*, 2623.
[73] Q. Jiang, Y. Zhao, X. Zhang, X. Yang, Y. Chen, Z. Chu, Q. Ye, X. Li, Z. Yin, J. You, *Nat Photonics* **2019**, *13*, 460.

[74] Q. Jiang, Z. Chu, P. Wang, X. Yang, H. Liu, Y. Wang, Z. Yin, J. Wu, X. Zhang, J. You, *Advanced Materials* **2017**, *29*, 1703852.
[75] Z. Hu, Q. An, H. Xiang, L. Aigouy, B. Sun, Y. Vaynzof, Z. Chen, *ACS Appl Mater Interfaces* **2020**, *12*, 54824.

Table of Contents (TOC) text and graphic

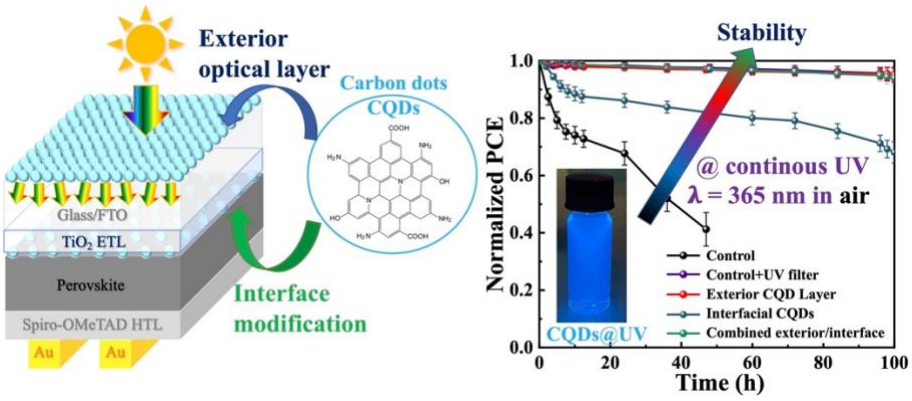

By harvesting both the optical and the structural properties of bottom-up-synthesized colloidal carbon quantum dots (CQDs), we provide a cost-effective means to circumvent the UV-induced degradation in efficient perovskite solar cells (PSCs) without scarification on their power conversion efficiencies (PCEs).